







## Structural evolution and $K$ mixing in $^{49}\text{V}$

Y. Sapkota <sup>1</sup>, Rozina Rahaman,<sup>1</sup> Abhijit Bisoi <sup>1,\*</sup>, Anik Adhikari,<sup>1</sup> Arkabrata Gupta,<sup>1</sup> Ananya Das,<sup>1</sup> H. Ghosh,<sup>1</sup> S. Sarkar,<sup>1</sup> Dibyadyuti Pramanik,<sup>2</sup> Sangeeta Das,<sup>3</sup> Sathi Sharma,<sup>3</sup> S. Ray,<sup>4</sup> S. Rajbanshi,<sup>5</sup> Shabir Dar <sup>6,7</sup>, S. Nandi <sup>6,7</sup>, S. Bhattacharya,<sup>6,7</sup> T. Bhattacharjee <sup>6,7</sup>, G. Mukherjee,<sup>6,7</sup> S. Bhattacharyya <sup>6,7</sup>, S. Samanta,<sup>8</sup> S. Das,<sup>8</sup> S. Chatterjee,<sup>8</sup> R. Raut,<sup>8</sup> and S. S. Ghugre<sup>8</sup>

<sup>1</sup>Indian Institute of Engineering Science and Technology, Shibpur, Howrah 711103, India

<sup>2</sup>Haldia Institute of Technology, Haldia 721631, India

<sup>3</sup>Saha Institute of Nuclear Physics, Bidhannagar, Kolkata 700064, India

<sup>4</sup>Amity Institute of Nuclear Science and Technology, Amity University, Noida, India

<sup>5</sup>Presidency University, Kolkata 700073, India

<sup>6</sup>Variable Energy Cyclotron Centre, 1/AF Bidhannagar, Kolkata 700064, India

<sup>7</sup>Homi Bhabha National Institute, Training School Complex, Anushaktinagar, Mumbai 400094, India

<sup>8</sup>UGC-DAE Consortium for Scientific Research, Kolkata Centre, Kolkata 700098, India



(Received 18 August 2021; revised 8 December 2021; accepted 10 March 2022; published 7 April 2022)

Lifetimes of a few negative parity levels and multipole mixing ratios ( $\delta$ ) for a few dipole transitions in  $^{49}\text{V}$ , populated through the  $^{48}\text{Ti}(^4\text{He}, 2np)^{49}\text{V}$  reaction with a 48 MeV  $^4\text{He}$  beam, were measured. The Indian National Gamma Array (INGA) facility was used to detect  $\gamma$  rays at three different angles. Large basis shell model calculations were performed to understand the microscopic origin of these levels and to interpret the observations.  $K$  mixing between different  $K$  bands in  $^{49}\text{V}$  were established from one-nucleon-transfer spectroscopic factor calculations and total Routhian surface (TRS) calculations.

DOI: [10.1103/PhysRevC.105.044304](https://doi.org/10.1103/PhysRevC.105.044304)

### I. INTRODUCTION

The study of  $1f_{7/2}$  shell nuclei has generated new interest due to the recent employment of sophisticated techniques of  $\gamma$  spectroscopy. The total number of valence particles/holes in the  $1f_{7/2}$  shell is 16, and near the middle of the  $1f_{7/2}$  shell the number of valence particles/holes  $\approx 8$ , which is large enough to lead to a collective behavior. Collectivity in the ground state, therefore, increases towards the middle of the  $1f_{7/2}$  shell, and starts to disappear rapidly while approaching the doubly magic nucleus  $^{56}\text{Ni}$ , as nuclei evolve towards a spherical shape [1–5].  $^{48}\text{Cr}$  was one of the earliest nuclei to be studied in this regard, due to the presence of eight valence nucleons outside the  $^{40}\text{Ca}$  core. Strong collectivity has been observed near the ground state in  $^{48}\text{Cr}$  [3–9]. Rotational-like band structures have been observed in a few nuclei around  $^{48}\text{Cr}$  also [9,10]. Shape transitions towards triaxial and non-collective deformations have been observed in these nuclei at higher spins due to the alignment of valence nucleons in the  $1f_{7/2}$  shell [11]. Band terminating states, corresponding to fully aligned  $1f_{7/2}$  configurations and back-bending phenomena have also been observed in a few  $1f_{7/2}$  nuclei [2,3], and have been explained successfully by shell model calculations [12–14]. Another comprehensive shell model description of  $1f_{7/2}$  nuclei can be found in Ref. [15].

$^{49}\text{V}$  has 9 nucleons (3 protons + 6 neutrons) in the  $1f_{7/2}$  orbital.  $^{49}\text{V}$  populated through a heavy-ion-induced reaction

was previously studied by Rodrigues *et al.* [16]. They extended the level scheme up to 13 MeV, and assigned the spins and parities of most of the levels. They established the  $K^\pi = 3/2^-$  negative parity yrast band and a  $K^\pi = 15/2^-$  sideband up to the band terminating  $27/2^-$  state. But they did not measure the lifetimes of these levels. Recently, Mukhopadhyay *et al.* [17] investigated the yrast and a few non-yrast negative parity levels in  $^{49}\text{V}$ , populated through the heavy-ion-induced  $^{27}\text{Al}(^{28}\text{Si}, \alpha 2p)^{49}\text{V}$  reaction. They measured the lifetimes of  $15/2_1^-$ ,  $19/2_1^-$ ,  $23/2_1^-$ ,  $25/2_1^-$ , and  $27/2_1^-$  levels of the  $K^\pi = 3/2^-$  negative parity yrast band. In the same work, they measured the lifetimes of  $15/2_2^-$  and  $17/2_1^-$  levels of the  $K^\pi = 15/2^-$  sideband also. Lifetimes of two other members of the  $K^\pi = 15/2^-$  band ( $19/2_2^-$  and  $21/2_1^-$ ) are, however, still unknown. Lifetimes of a few other negative parity levels (viz., 5856 and 6465 keV) are also not known to us. They also studied the variation of spectroscopic quadrupole moment  $Q_s$  for the  $K^\pi = 3/2^-$  and  $15/2^-$  bands. The change in  $Q_s$  for the ground state band was explained in terms of mixing of the observed  $K^\pi = 3/2^-$  and  $K^\pi = 15/2^-$  bands. However, no quantitative analysis was performed to study the nature and extent of this mixing along the two bands. An explanation of the sudden change of  $Q_s$  at  $J = 19/2_2^-$  in the  $K^\pi = 15/2^-$  band [15] was also not provided in that work. Therefore, the primary motivation of our work is to measure the lifetimes of these negative parity levels, and study the evolution of nuclear structure and  $K$  mixing with angular momentum in  $^{49}\text{V}$ .

In the present work, we measured the lifetimes of four negative parity levels in  $^{49}\text{V}$  for the first time and remeasured the lifetimes of a few negative parity levels to validate our

\* abhijitbisoi@physics.iests.ac.in

measurements. Multipole mixing ratios ( $\delta$ ) of a few dipole transitions were also measured for the first time. Large basis shell model (LBSM) calculations were performed to understand the microscopic origin of the negative parity levels. One-nucleon-transfer spectroscopic factors were extracted using LBSM calculations to understand the  $K$  mixing between the levels of interest, and to interpret the observations.

In the following sections, we discuss in detail the experiment, data analysis techniques, experimental results, and theoretical investigations.

## II. EXPERIMENTAL DETAILS

High spin states of  $^{49}\text{V}$  were populated through the  $^{48}\text{Ti}(^4\text{He}, 2np)^{49}\text{V}$  fusion evaporation reaction at  $E_{lab} = 48$  MeV. The  $^4\text{He}$  beam was provided by the K-130 Cyclotron at Variable Energy Cyclotron Centre (VECC) Kolkata. The experiment was carried out on a self-supported 12.4 mg/cm<sup>2</sup> thick natural Ti target, where  $\approx 95\%$  of the recoils stopped within the target. A multidetector array (INGA setup), comprising six Compton suppressed clovers and two low energy photon spectrometers (LEPS), was used to detect the  $\gamma$  rays. These six clovers were mounted at three different angles, viz., 125°(2), 90°(3), and 40°(1) with respect to the beam axis. Two LEPS were mounted at 90° and 40° with respect to the beam axis. About  $10^9$  twofold  $\gamma$ - $\gamma$  coincidence events were recorded in list mode using a digital data acquisition system. The pulse processing and data acquisition system was that of UGC-DAE CSR, Kolkata Centre, and was based on 250 MHz 12-bit PIXIE 16 digitizers (XIA LLC) [18]. The raw data were sorted using the program IUCPIX [18] to generate symmetric and asymmetric matrices, which were then analyzed using the program INGASORT [19].

The energy calibrations of the clovers were performed with  $^{152}\text{Eu}$  and  $^{133}\text{Ba}$  radioactive sources. These sources emit  $\gamma$  rays having energies up to 1408 keV only. The high energy room background  $\gamma$ 's (like 2614 keV) also could not be considered for energy calibration due to their low statistics. So, we used a few online  $\gamma$ 's with energy ranging from 400 through 2100 keV for energy calibration and for estimating the corresponding uncertainties in the high energy region. The relative efficiency calibrations of the clovers were performed with  $^{152}\text{Eu}$  and  $^{66}\text{Ga}$  radioactive sources. The  $^{66}\text{Ga}$  source with  $\gamma$  energies ranging from 833 to 4806 keV was prepared through the  $^{56}\text{Fe}(^{13}\text{C}, p2n)^{66}\text{Ga}$  reaction at 50 MeV [20]. The efficiency uncertainty was estimated by fitting the efficiency curve in INGASORT [19].

## III. RESULT AND DISCUSSION

### A. Level scheme

The negative parity levels in  $^{49}\text{V}$  were investigated through the angle-dependent (90° vs 90°) symmetric and asymmetric matrices. A total projection spectrum as well as a typical gated spectrum are shown in Fig. 1. As we used a natural Ti target, the cross section of  $^{49}\text{V}$  as predicted from PACE4 [21] is 34.6% of the total cross section. We therefore included the various nuclei populated in the present experiment in Fig. 1(a). In the figure, only the strongest ground state transitions of the popu-

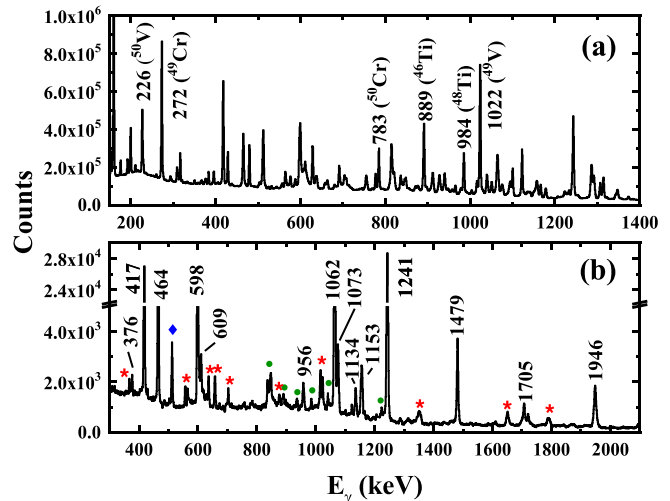


FIG. 1. (a) A total projection spectrum of  $\gamma$  rays emitted by different nuclei formed in the present experiment. (b) Background subtracted coincidence spectrum obtained by putting a gate on the 1022 keV transition. These spectra were generated from 90° vs 90° symmetric matrices. Transitions not relevant to the present work are marked with red asterisks. Transitions marked with green circles are contaminant peaks. The transition marked with a blue diamond is the 511 keV annihilation peak.

lated nuclei are marked. In the present experiment, almost all the existing transitions up to  $J^\pi = 27/2^-$  [16] were observed. Transitions above the 7797 keV ( $27/2^-$ ) level could not be identified due to their low statistics. The levels relevant to the present work are shown in Fig. 2. Due to the presence of Doppler broadening in most of the transitions, we measured the relative intensities (Table I) and branching ratios (Table II) of all these transitions from a 90° vs 90° symmetric

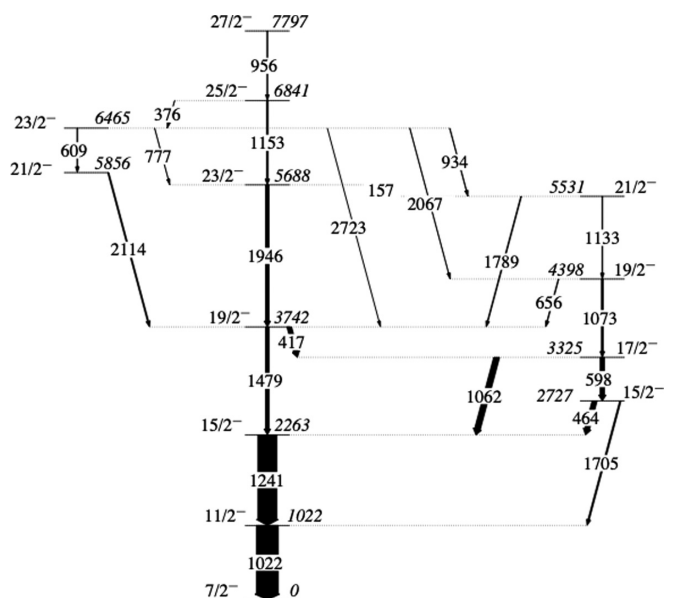


FIG. 2. Partial level scheme of  $^{49}\text{V}$ . Only the levels of interest are shown in this figure.

TABLE I. Relative intensity ( $I_{\text{rel}}$ ),  $R_{\text{DCO}}$ ,  $\Delta_{\text{IPDCO}}$ , and mixing ratio ( $\delta$ ) of  $\gamma$  transitions in  $^{49}\text{V}$ .

$E_\gamma$ (keV)	$I_{\text{rel}}$	$J_i$	$J_f$	Gating $\gamma$		$R_{\text{DCO}}$	Mixing ratio ( $\delta$ )			$\Delta_{\text{IPDCO}}$ Expt.
				$E$ (keV)	$\Delta J$		Present	Prev.	Theor.	
417(1)	21.0(14)	19/2 <sub>1</sub> <sup>-</sup>	17/2 <sub>1</sub> <sup>-</sup>	1022	2	0.66(5)	-0.05 <sup>+0.07</sup> <sub>-0.09</sub>	-0.04(2) <sup>a</sup>	-0.03	-0.07(1)
464(1)	22.6(8)	15/2 <sub>2</sub> <sup>-</sup>	15/2 <sub>1</sub> <sup>-</sup>	1022	2	1.03(7)	-0.04 <sup>+0.12</sup> <sub>-0.09</sub>	> -0.10, <0.04 <sup>b</sup>	-0.04	0.15(1)
598(1)	19.7(13)	17/2 <sub>1</sub> <sup>-</sup>	15/2 <sub>2</sub> <sup>-</sup>	1022	2	0.67(5)	-0.03 <sup>+0.07</sup> <sub>-0.08</sub>		-0.04	-0.04(1)
609(1)	3.3(3)	23/2 <sub>2</sub> <sup>-</sup>	21/2 <sub>2</sub> <sup>-</sup>	1022	2	0.68(7)	-0.05(11)		-0.02	-0.02(1)
956(1)	2.7(3)	27/2 <sub>1</sub> <sup>-</sup>	25/2 <sub>1</sub> <sup>-</sup>	1022	2	0.70(10)	-0.03 <sup>+0.15</sup> <sub>-0.17</sub>		-0.03	-0.03(2)
1022(1)	100.0(33)	11/2 <sub>1</sub> <sup>-</sup>	7/2 <sub>1</sub> <sup>-</sup>	1946	2	1.00(8)	$E2$	$E2$	$E2$	0.10(1)
1062(1)	26.3(17)	17/2 <sub>1</sub> <sup>-</sup>	15/2 <sub>1</sub> <sup>-</sup>	417	1	0.90(6)	-0.04(11)		-0.06	-0.04(1)
1073(1)	8.0(6)	19/2 <sub>2</sub> <sup>-</sup>	17/2 <sub>1</sub> <sup>-</sup>	598	1	1.00(10)	-0.03 <sup>+0.14</sup> <sub>-0.17</sub>		-0.08	-0.04(1)
1133(1)	2.9(3)	21/2 <sub>1</sub> <sup>-</sup>	19/2 <sub>2</sub> <sup>-</sup>	1022	2	0.66(9)	-0.07 <sup>+0.12</sup> <sub>-0.14</sub>		-0.06	-0.06(2)
1153(1)	7.2(5)	25/2 <sub>1</sub> <sup>-</sup>	23/2 <sub>1</sub> <sup>-</sup>	1022	2	0.65(6)	-0.10 <sup>+0.07</sup> <sub>-0.08</sub>		-0.06	-0.01(1)
1241(1)	86.0(29)	15/2 <sub>1</sub> <sup>-</sup>	11/2 <sub>1</sub> <sup>-</sup>	1022	2	1.01(7)	$E2$	$E2$	$E2$	0.08(1)
1479(1)	16.6(7)	19/2 <sub>1</sub> <sup>-</sup>	15/2 <sub>1</sub> <sup>-</sup>	1022	2	0.97(8)	$E2$	$E2$	$E2$	0.08(1)
1705(1)	6.1(3)	15/2 <sub>2</sub> <sup>-</sup>	11/2 <sub>1</sub> <sup>-</sup>	1022	2	0.97(11)	$E2$	$E2$	$E2$	0.04(2)
1946(1)	15.7(7)	23/2 <sub>1</sub> <sup>-</sup>	19/2 <sub>1</sub> <sup>-</sup>	1022	2	0.98(9)	$E2$	$E2$	$E2$	0.06(1)
2067(2)	1.1(3) <sup>c</sup>	23/2 <sub>2</sub> <sup>-</sup>	19/2 <sub>2</sub> <sup>-</sup>							
2114(1)	5.3(5)	21/2 <sub>2</sub> <sup>-</sup>	19/2 <sub>1</sub> <sup>-</sup>	1479	2	0.60(9)	-0.17 <sup>+0.15</sup> <sub>-0.20</sub>		-0.17	-0.03(2)
2723(2)	0.4(3) <sup>c</sup>	23/2 <sub>2</sub> <sup>-</sup>	19/2 <sub>1</sub> <sup>-</sup>							

<sup>a</sup>From Ref. [17].<sup>b</sup>From Ref. [23].<sup>c</sup>From branching.

matrix. Necessary correction due to the angular distributions of dipole and quadrupole transitions at  $90^\circ$  was taken care of

TABLE II. Comparison of experimental and theoretical branching ratios of different excited levels.

Energy (keV)		Branching ratio		
Level	$\gamma$	Expt.		Theor.
		Present	Prev. <sup>a</sup> [16]	
2727	464	78(3)	80(3)	78
	1705	22(3)	20(3)	22
3325	598	34(5)	40(1)	36
	1062	66(5)	60(1)	64
3742	417	59(4)	68(2)	58
	1479	41(4)	32(2)	42
4398	656	26(6)	29(3)	25
	1073	74(6)	71(3)	75
5531	1133	78(7)	75(5)	72
	1789	22(7)	25(5)	28
5688	157	6(4)	10(2)	3
	1946	94(4)	90(2)	97
6465	609	47(4)	41(4)	45
	777	6(1)	15(4)	4
	934	26(3)	25(4)	23
	2067	15(2)	10(4)	18
	2723	6(1)	9(4)	10
6841	376	9(7)	13(3)	9
	1153	91(7)	87(3)	91

<sup>a</sup>Estimated from relative intensities.

in these measurements. The measured branching ratios agree well with the results obtained from shell model calculations. The present results are also in reasonable agreement with the previously measured branchings [16]. Since the previous branchings were estimated from their reported intensities, measured from an all-angle symmetry matrix, deviations of more than 10% were found for a few transitions. The measured relative intensities and the branchings were then used in line-shape analysis subsequently.

The multipole mixing ratios ( $\delta$ ) of most of the dipole transitions in  $^{49}\text{V}$  are not known. We therefore performed measurements of directional correlations of  $\gamma$  rays deexciting oriented states (DCO) to determine the multipole mixing ratios ( $\delta$ ) of the dipole transitions. The DCO ratio ( $R_{\text{DCO}}$ ) is defined as

$$R_{\text{DCO}} = \frac{I^{\gamma_1} \text{ observed at angle } \theta, \text{ gated by } \gamma_2 \text{ at } 90^\circ}{I^{\gamma_1} \text{ observed at angle } 90^\circ, \text{ gated by } \gamma_2 \text{ at } \theta}$$

The DCO ratios were determined here for  $\theta = 125^\circ$ . For the present setup, the DCO value for stretched transitions of the same multipolarity is close to unity, and for a stretched dipole (quadrupole) transition gated by a pure quadrupole (dipole), it is nearly 0.7 (1.5).

The measured  $R_{\text{DCO}}$  values of most of the dipole transitions (Table I) are then compared with theoretical values calculated using the computer code ANGCOR [22] to extract  $\delta$  values. Spin alignment parameter  $\sigma/J = 0.31^{+0.06}_{-0.05}$  was estimated from the measured  $R_{\text{DCO}}$  of the 1139 keV  $E2$  transition, gated by the 1512 keV  $E1$  transition.

We measured the multipole mixing ratios ( $\delta$ ) of eight magnetic dipole transitions in  $^{49}\text{V}$  (Table I) for the first time. We

also remeasured the  $\delta$ 's of 417 and 464 keV transitions. The measured  $\delta$  of the 417 keV transition is  $-0.05_{-0.09}^{+0.07}$ , which agrees well with its reported value of  $-0.04(2)$  [16]. The reported value of the  $\delta$  of the 464 keV transition was  $> -0.10$ ,  $< 0.04$  [23]. In the present work, we obtained  $\delta = -0.04_{-0.09}^{+0.12}$  for this transition. Our measured values of  $\delta$  agree well with the  $\delta$ 's obtained from shell model calculations also (Table I).

The parities of all the excited levels of interest in  $^{49}\text{V}$  were confirmed from measurements of the integrated polarization directional correlation of oriented nuclei (IPDCO) [24]. The results are shown in Table I. A positive value of  $\Delta_{IPDCO}$  implies a pure electric transition, whereas its negative value indicates a pure magnetic transition. In the case of  $\Delta J = 0$  transitions, the scenario is reversed, and a positive (negative) value of  $\Delta_{IPDCO}$  indicates the magnetic (electric) nature of the transition [25]. For a mixed transition, the value is close to zero, and the sign depends on the amount of mixing.

Uncertainties quoted in the measured values of intensities and branching ratios (Tables I and II) are inclusive of statistical errors, efficiency correction, and angular distribution correction for the intensities measured with the  $90^\circ$  detectors. For  $R_{DCO}$ , uncertainties due to statistical errors and efficiency correction were considered. Uncertainties quoted in the measured values of  $\Delta_{IPDCO}$  are statistical only.

## B. Lifetime measurements

To understand the structural evolution in  $^{49}\text{V}$ , the level lifetimes of  $K^\pi = 3/2^-$  and  $K^\pi = 15/2^-$  band members are required. The lifetimes of 2263 keV ( $15/2_1^-$ ), 2727 keV ( $15/2_2^-$ ), 3325 keV ( $17/2_1^-$ ), 3742 keV ( $19/2_1^-$ ), 5688 keV ( $23/2_1^-$ ), 6841 keV ( $25/2_1^-$ ), and 7797 keV ( $27/2_1^-$ ) levels were recently measured through heavy-ion-induced reactions by Mukhopadhyay *et al.* [17]. However, they did not measure the lifetimes of 4398 keV ( $19/2_2^-$ ) and 5531 keV ( $21/2_1^-$ ) levels in the  $K^\pi = 15/2^-$  band. In the present work, we extracted the lifetimes of these levels from line-shape analysis. The modified version of the computer code LINESHAPE [26] was used to extract the level lifetime from Doppler-shifted spectra. The initial recoil momenta distributions of  $^{49}\text{V}$  were obtained from PACE4 [21] calculation. In the first step of the LINESHAPE program, the slowing-down histories of 50 000  $^{49}\text{V}$  recoiling nuclei in the natural Ti target were simulated using the Monte Carlo technique. The velocity profiles of the recoils were generated with a time step of 0.0007 ps. The detector geometry was also taken into account. In the second step, using the stopping powers and the velocity distributions calculated in the first step, a line-shape for each decay time was obtained. In the final step, utilizing a  $\chi^2$ -minimization technique, the theoretically generated line shapes best fitted to the experimental ones were obtained. The  $\gamma$  transition energies and the side-feeding intensities obtained from the measured relative intensities were used as the input parameters to extract the level lifetime. In this measurement, shell-corrected Northcliffe and Schilling stopping powers [27] were used to calculate the energy loss of ions in matter.

The lifetime measurements of 4398 and 5531 keV levels were carried out from the line-shape spectra of 1073 and 1133 keV transitions, respectively (Fig. 3). Due to low statistics and

contaminant peaks, lineshape spectra of these two transitions were generated by putting gates on a transition below the transitions of interest (GTB) for  $125^\circ$  and  $90^\circ$  only. While using GTB for lifetime measurements, it is very important to consider proper side feeding. In the present work, therefore, the side-feeding was modeled with a cascade of five transitions. The dynamic moment of inertia of this side-feeding band is taken to be  $8.3 \text{ MeV}^{-1} \hbar^2$ , the same as that of the band under consideration [26]. The side-feeding intensities were estimated from the relative intensities of the feeding and decay out transitions. Starting with the 1133 keV transition, we sequentially fitted the 1073 keV transition. After having fitted these two transitions, a global least-squares minimization was carried out for these two transitions simultaneously. During each line-shape simulation, the transition quadrupole moments ( $Q_i$ ), the side-feeding quadrupole moments ( $Q_{i,s}$ ), background parameters, and intensities of contaminant peaks for each level were kept as free parameters.

We also observed large Doppler shifts for two intense 609 and 2114 keV transitions decaying from 6465 keV ( $23/2_2^-$ ) and 5856 keV ( $21/2_2^-$ ) levels, respectively. The 2114 keV transition is directly fed to the  $K^\pi = 3/2^-$  band. Similarly, four other transitions from 6465 keV ( $23/2_2^-$ ) level are directly fed to the  $K^\pi = 3/2^-$  and  $K^\pi = 15/2^-$  bands (Fig. 2). The lifetimes of these levels are, therefore, also important to understand the evolution of nuclear structure with angular momentum in  $^{49}\text{V}$ . Hence, we measured the lifetimes of 5856 keV ( $21/2_2^-$ ) and 6465 keV ( $23/2_2^-$ ) levels using the same procedure as discussed above. We analyzed the line-shape spectra of 609 and 2114 keV transitions for  $125^\circ$  and  $90^\circ$  to extract the lifetimes of these levels (Fig. 3). These spectra were generated by putting gates on the 1022 keV transition. The measured lifetimes of 5856 and 6465 keV levels are close to the lifetimes that were obtained for the levels with similar excitation energies in  $K^\pi = 3/2^-$  and  $K^\pi = 15/2^-$  bands (Table III).

In the present work, we also remeasured the lifetimes of other members of  $K^\pi = 3/2^-$  and  $K^\pi = 15/2^-$  bands (Figs. 3 and 4) and compared them with their reported values [17]. The results are shown in Table III. Except for the 2263 keV level, the results agree well. We found that several lifetimes ( $\tau_m = 0.045$  to  $> 3.84$  ps) of the 2263 keV level have been reported in the literature [23,28–30], and the latest measurement by Mukhopadhyay *et al.* [17] agrees well with the earlier lifetime reported by Hass *et al.* [23]. However, in the present work, the measured lifetime of 2263 keV level is almost double its recently reported value [17]. This may be due to the presence of more than one strong fast-feeding transition. The 2263 keV level is fed by three strong transitions, viz., 464, 1062, and 1479 keV, and all of them have Doppler shapes. So, during line-shape analysis, one has to consider these feeding transitions in the feeding history of the 2263 keV level. In the present work, we therefore used the intensity weighted average of the level lifetimes of 2727, 3325, and 3742 keV levels to determine the lifetime of the 2263 keV level from the line-shape spectra of the 1241 keV transition. Similarly, the intensity weighted average of the level lifetimes of 3742 and 4398 keV levels were used as the feeding time to extract the lifetime of the 3325 keV level.

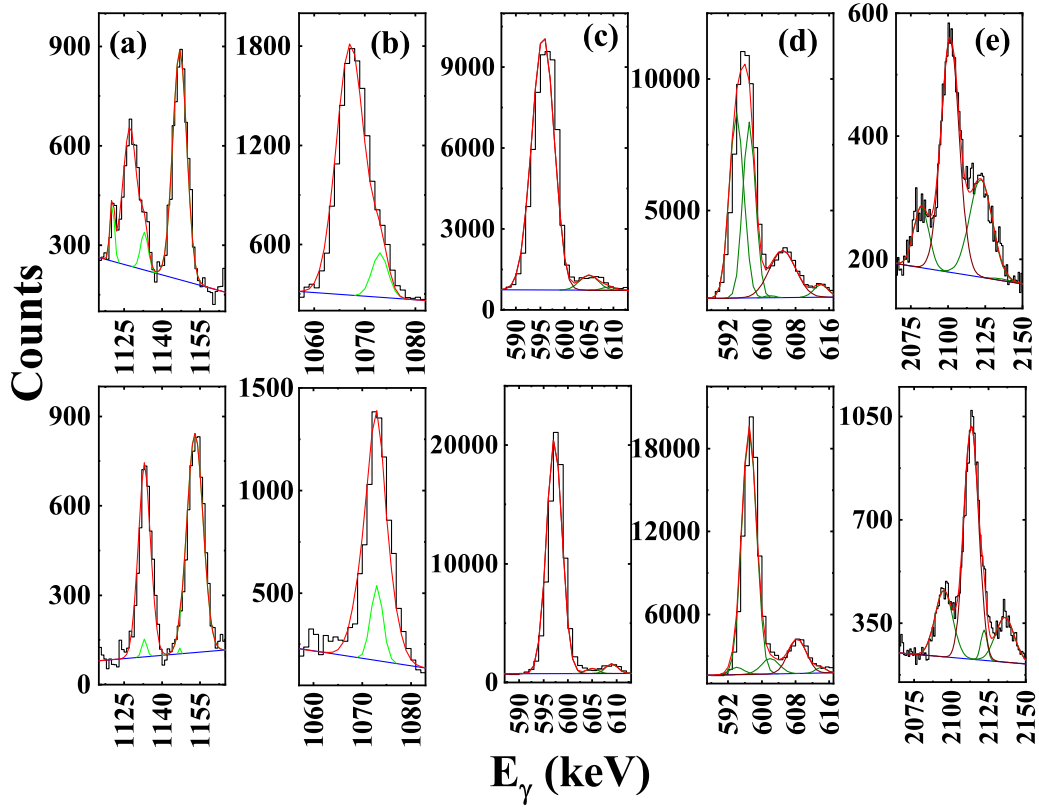


FIG. 3. Experimental (black) and simulated (red) line-shape spectra are shown for (a) 1133, (b) 1073, (c) 598, (d) 609, and (e) 2114keV transitions for two different angles,  $125^\circ$  (top) and  $90^\circ$  (bottom). Stopped peaks are shown in green.

The quoted errors in the measured lifetimes were estimated from the behavior of the  $\chi^2$  fit in the vicinity of the minimum, stopping power uncertainties, and the continuous production and stopping of the recoils in the thick target and vacuum. However, in the reported lifetimes of Ref. [17], errors due to stopping power were not considered.

The experimental  $B(M1)$  and  $B(E2)$  values were then determined from these measured lifetimes. The branching ratios and the mixing ratios were taken from the present measurements. The results are shown in Table III.

#### IV. THEORETICAL CALCULATION

Large basis shell model (LBSM) calculations were performed using the code NUSHELLX [31] to understand the microscopic origin of the levels of interest in  $^{49}\text{V}$ . The KB3GPN effective interaction [32], developed for the  $fp$  major shell above the  $^{40}\text{Ca}$  core, was used for the present calculations. The valence space consists of  $1f_{7/2}$ ,  $1f_{5/2}$ ,  $2p_{3/2}$ , and  $2p_{1/2}$  orbitals for both protons and neutrons. The number of valence particles in  $^{49}\text{V}$  is 9 (3 protons + 6 neutrons). No restriction was applied on any particle to generate the levels. The results are shown in Fig. 5. The calculated energies of the levels of interest are in good agreement with their experimental energies. The following section discusses our experimental and theoretical results in detail.

#### V. EVOLUTION OF NUCLEAR STRUCTURE WITH ANGULAR MOMENTUM

In the present work, we studied the evolution of nuclear structure with angular momentum for the  $K^\pi = 3/2^-$  and  $K^\pi = 15/2^-$  bands, and two other negative parity levels of  $^{49}\text{V}$ . The investigation was carried out based on the measured transition strengths of the transitions decaying from the levels of interest and on the results obtained from shell model calculations.

##### A. Configuration mixing and deformation

The decomposition of the wave functions for the negative parity levels in  $^{49}\text{V}$  are shown in Table IV. The probability and the structure of different partitions having more than 10% contribution are listed in the table. The partitions are given in terms of occupation numbers of valence single-particle states. In the table,  $N$  is the total number of particle partitions for a particular level.

It is seen from Table IV that all the negative parity levels have a much smaller extent of configuration mixing. It was found that the low lying levels have comparatively larger configuration mixing in terms of single-particle partitions. The configuration mixing shows a decreasing trend with increasing angular momenta. The minimum configuration mixing with the most significant contribution from a single partition ( $\approx 82\%$ ) was obtained for the  $27/2^-_1$  level, which is the band terminating state of the observed negative parity yrast band.

TABLE III. Experimental level lifetimes and experimental and theoretical reduced transition probabilities [ $B(L)$ ] for different transitions are tabulated. The units of  $B(M1)$  and  $B(E2)$  are  $\mu_N^2$  and  $e^2\text{fm}^4$  respectively. The  $B(M1)$  values quoted as upper limits are calculated assuming pure  $M1$  transitions.

$E_x$ (keV)	$\tau_{\text{mean}}$ (ps)		$J_i^\pi$	$J_f^\pi$	$E_\gamma$ (keV)	$B(M1)$		$B(E2)$	
	Present	Prev. [17,23]				Expt.	Theor.	Expt.	Theor.
For $K^\pi = 3/2^-$ band									
1022		5.1(1)	$11/2_1^-$	$7/2_1^-$	1022			140(32)	183
2263	1.61(47)	0.92(14)	$15/2_1^-$	$11/2_1^-$	1241			169(55)	165
3742	0.37(10)	0.38(4)	$19/2_1^-$	$15/2_1^-$	1479			125(48)	90
			$19/2_1^-$	$17/2_1^-$	417	1.23(42)	0.86		
5688	0.32(8)	0.31(3)	$23/2_1^-$	$19/2_1^-$	1946			84(24)	99
			$23/2_1^-$	$21/2_1^-$	157	<2.7(24)	1.4		
6841	0.07(2)	0.09(2)	$25/2_1^-$	$23/2_1^-$	1153	0.48(16)	0.54		
7797	<0.03(1)	0.05(1)	$27/2_1^-$	$25/2_1^-$	956	>1.88(68)	2.13		
For $K^\pi = 15/2^-$ band									
2727	0.34(9)	0.41(6)	$15/2_2^-$	$15/2_1^-$	464	1.28(37)	1.41		
			$15/2_2^-$	$11/2_1^-$	1705			35(13)	40
3325	0.07(2)	0.08(1)	$17/2_1^-$	$15/2_2^-$	598	1.30(51)	1.40		
			$17/2_1^-$	$15/2_1^-$	1062	0.45(15)	0.44		
4398	0.07(2)		$19/2_2^-$	$17/2_1^-$	1073	0.43(17)	0.64		
			$19/2_2^-$	$19/2_1^-$	656	<0.71(33)	0.93		
5531	0.09(2)		$21/2_1^-$	$19/2_2^-$	1133	0.35(11)	0.37		
			$21/2_1^-$	$19/2_1^-$	1789	<0.03(1)	0.04		
5856	0.06(1)		$21/2_2^-$	$19/2_1^-$	2114	0.10(3)	0.32		
6465	0.11(2)		$23/2_2^-$	$21/2_2^-$	609	1.10(37)	1.42		
			$23/2_2^-$	$23/2_1^-$	777	<0.07(2)	0.06		
			$23/2_2^-$	$21/2_1^-$	934	<0.17(6)	0.20		
			$23/2_2^-$	$19/2_2^-$	2067			29(9)	51
			$23/2_2^-$	$19/2_1^-$	2723			3(1)	7

The proton and neutron average occupation numbers of the  $1f_{7/2}$ ,  $2p_{3/2}$ ,  $1f_{5/2}$ , and  $2p_{1/2}$  orbitals obtained from shell model calculations were also plotted for the  $K^\pi = 3/2^-$  and  $K^\pi = 15/2^-$  bands and two other negative parity levels of  $^{49}\text{V}$  in Fig. 6. It is seen from Fig. 6 that the  $1f_{7/2}$  orbital is the most occupied one for all three bands. However, while describing these negative parity levels microscopically, the contribution from the other three orbitals cannot be ignored completely, as pointed out in [33].

The  $B(M1)$  and  $B(E2)$  strengths of the decay out transitions were also derived from the calculated wave functions of the levels of interest. In this calculation, effective charges  $e_p = 1.5e$  and  $e_n = 0.5e$  [34] and the free values of  $g$  factors were used. In Figs. 7 and 8, we compare the calculated  $B(E2)$  and  $B(M1)$  strengths with their present experimental values and also with earlier measurements wherever available. For the  $K^\pi = 3/2^-$  band, large  $B(E2)$  strengths (140–70  $e^2\text{fm}^4$ ) with a maximum deformation  $\beta_2 = 0.21$  were observed for low lying transitions up to the  $15/2_1^-$  level, above which the  $B(E2)$  values decrease.

For the  $K^\pi = 15/2^-$  band, large  $B(M1)$  transition strengths ( $\approx 1.3\mu_N^2$ ) were observed for low lying transitions up to the  $17/2_1^-$  level [Fig. 8 (a)]. Above the  $17/2_1^-$  level, the transition strengths of  $19/2_2^-$  and  $21/2_1^-$  levels fall suddenly to 0.3–0.4  $\mu_N^2$ . Since  $B(M1)$  reduced rates are indicators of single-particle features, we may conclude that the  $19/2_2^-$  and  $21/2_1^-$  levels are dominated by single-particle excitations, as

also suggested by the particle partitions (Table IV) obtained from shell model calculations. For the interband transitions, our theoretical results also agree with the experimental values within the uncertainty limits.

## B. One-nucleon-transfer spectroscopic factor calculation

In the present study, we also extracted spectroscopic quadrupole moments ( $Q_s$ ) and  $g$  factors of the levels of interest in  $^{49}\text{V}$  from their calculated wave functions (Fig. 9). The variation of  $Q_s$  for  $K^\pi = 3/2^-$  and  $15/2^-$  bands in  $^{49}\text{V}$  was also studied in Ref. [17,23]. In Ref. [17], the change in  $Q_s$  for the ground state band was explained in terms of mixing of the observed  $K^\pi = 3/2^-$  and  $K^\pi = 15/2^-$  bands. However, no quantitative analysis was performed for studying the nature and extent of this mixing along the two bands. An explanation of the sudden change of  $Q_s$  at  $J^\pi = 19/2_2^-$  in the  $K^\pi = 15/2^-$  band and the sudden change of  $Q_s$  from a positive value at  $J^\pi = 21/2_2^-$  to a negative value at  $23/2_2^-$  level was also not provided in that work.

In order to understand the variation of  $Q_s$  throughout the two bands in  $^{49}\text{V}$ , we studied its level structure and that of  $^{50}\text{Cr}$ , a well-studied neighboring nucleus. Brandolini *et al.* in Ref. [35] reported the coexistence of states with different  $K^\pi$  values in  $^{50}\text{Cr}$ . For the positive parity states in  $^{50}\text{Cr}$ , four bands corresponding to  $K^\pi = 0^+$ ,  $4^+$ ,  $6^+$ , and  $10^+$  were identified. The ground state band was assigned  $K^\pi = 0^+$ . The  $K^\pi = 4^+$

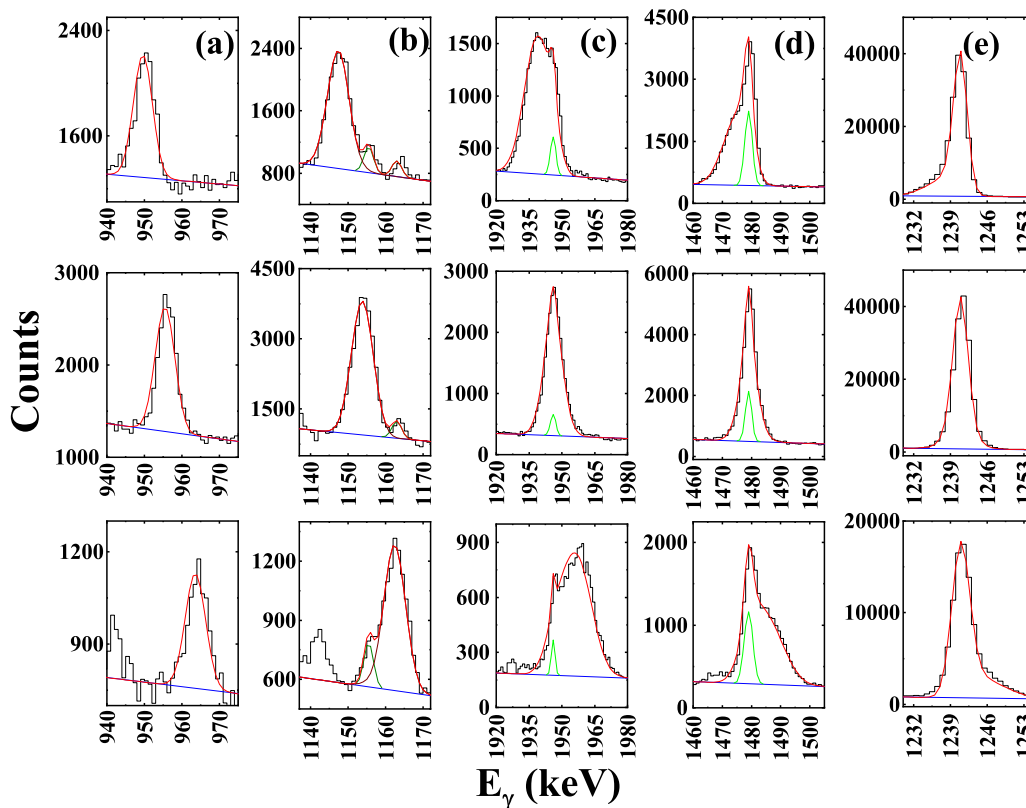


FIG. 4. Experimental (black) and simulated (red) line-shape spectra are shown for (a) 956, (b) 1153, (c) 1946, (d) 1479, and (e) 1241 keV transitions for three different angles, 125° (top), 90° (middle), and 40° (bottom). Stopped peaks are shown in green.

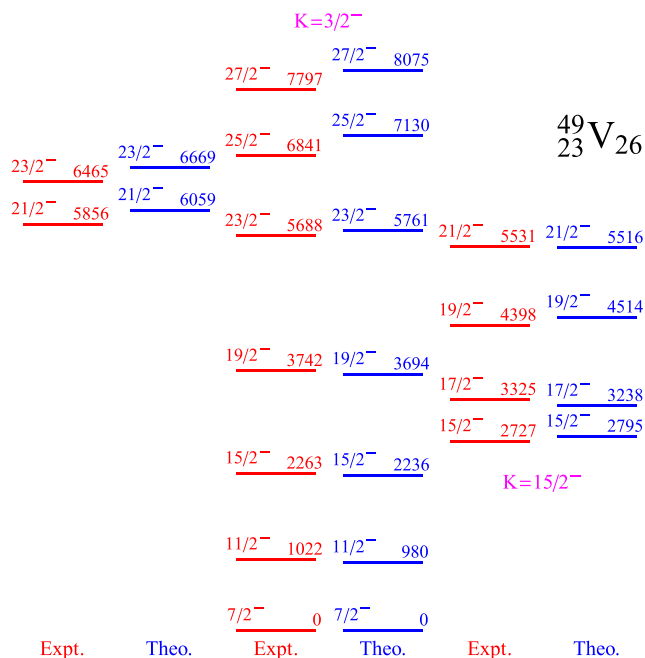


FIG. 5. Comparison of theoretical and experimental negative parity levels in <sup>49</sup>V. Only the levels of interest are shown in this figure.

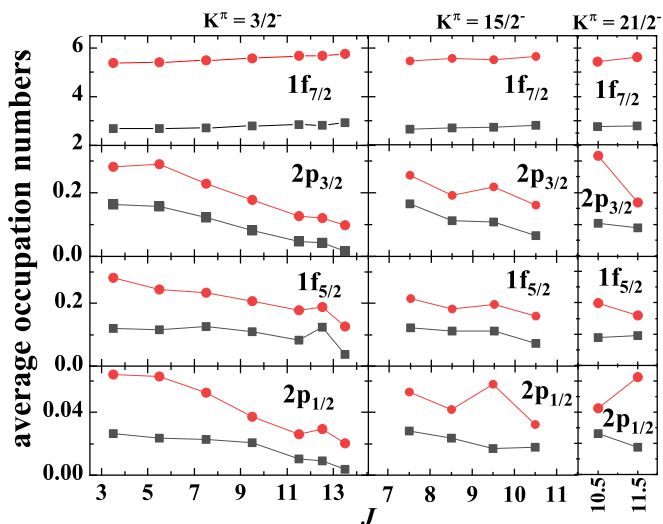


FIG. 6. Average occupation numbers of  $1f_{7/2}$ ,  $2p_{3/2}$ ,  $1f_{5/2}$  and  $2p_{1/2}$  orbitals (top to bottom panels) for the negative parity levels of the  $K^\pi = 3/2^-$ ,  $K^\pi = 15/2^-$  and  $K^\pi = 21/2^-$  bands (left to right panels) of <sup>49</sup>V. Note that the existence of the  $K^\pi = 21/2^-$  band is discussed in a later subsection. The proton and neutron occupation numbers are represented as red circles and grey squares, respectively. Data points are connected by lines to aid the eye.

TABLE IV. Structure of wave functions of the levels of interest in  $^{49}\text{V}$ . The partitions are given in terms of occupation numbers of the valence single-particle states in the following order:  $\pi 1f_{7/2}$ ,  $\pi 2p_{3/2}$ ,  $\pi 1f_{5/2}$ ,  $\pi 2p_{1/2}$ ,  $\nu 1f_{7/2}$ ,  $\nu 2p_{3/2}$ ,  $\nu 1f_{5/2}$ , and  $\nu 2p_{1/2}$ .  $\pi$  and  $\nu$  correspond to proton and neutron single-particle states, respectively.  $N$  is the total number of particle partitions that contribute to the corresponding level. Only those partitions are listed which contribute more than 10%.

$J_i^\pi$	Energy (keV)		Wave function		$N$
	Expt.	Theor.	%	Partition	
For $K^\pi = 3/2^-$ band					
$7/2_1^-$	0	0	49.70	[3,0,0,0,6,0,0,0]	94
$11/2_1^-$	1022	1036	49.75	[3,0,0,0,6,0,0,0]	87
$15/2_1^-$	2263	2324	54.3	[3,0,0,0,6,0,0,0]	87
$19/2_1^-$	3742	3841	60.93	[3,0,0,0,6,0,0,0]	76
$23/2_1^-$	5688	5917	70.04	[3,0,0,0,6,0,0,0]	59
$25/2_1^-$	6841	7209	65.15	[3,0,0,0,6,0,0,0]	42
$27/2_1^-$	7797	8213	81.81	[3,0,0,0,6,0,0,0]	26
For $K^\pi = 15/2^-$ band					
$15/2_2^-$	2727	2835	49.96	[3,0,0,0,6,0,0,0]	94
$17/2_1^-$	3325	3383	59.27	[3,0,0,0,6,0,0,0]	75
$19/2_2^-$	4398	4582	56.64	[3,0,0,0,6,0,0,0]	77
$21/2_1^-$	5531	5677	67.14	[3,0,0,0,6,0,0,0]	66
$21/2_2^-$	5856	6083	49.66	[3,0,0,0,6,0,0,0]	93
			16.46	[3,0,0,0,5,1,0,0]	
$23/2_2^-$	6465	6737	61.81	[3,0,0,0,6,0,0,0]	58

and  $K^\pi = 6^+$  bands were obtained by promoting a proton from the  $[321]3/2^-$  to the  $[312]5/2^-$  orbital and a neutron from the  $[312]5/2^-$  to the  $[303]7/2^-$  orbital, respectively, and by coupling the unpaired nucleons to the highest value

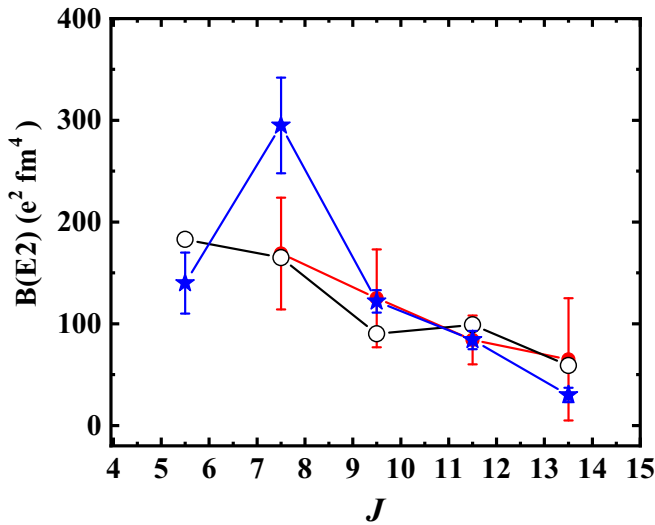


FIG. 7. Experimental (red) and calculated (black) transition strengths of the transitions in the  $K^\pi = 3/2^-$  band in  $^{49}\text{V}$ . Measured  $B(E2)$  values are also compared with the earlier measurements (blue) [17,23] wherever available. Data points are connected by lines to aid the eye.

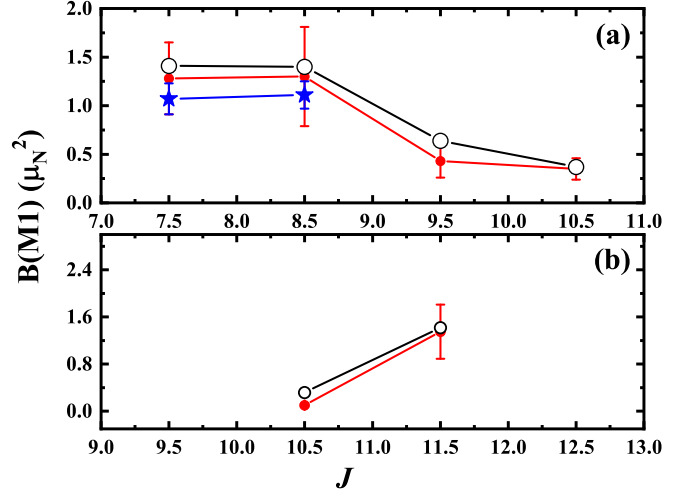


FIG. 8. Experimental (red) and calculated (black) transition strengths of the transitions (a) in  $K^\pi = 15/2^-$  band and (b) from 5856 and 6465 keV levels in  $^{49}\text{V}$ . Measured  $B(M1)$  values are also compared with the earlier measurements (blue) [17] wherever available. Data points are connected by lines to aid the eye.

of  $K$  [35]. Similarly, the  $K^\pi = 10^+$  band was obtained by the simultaneous recoupling of a proton pair to  $K^\pi = 4^+$  and of a neutron pair to  $K^\pi = 6^+$ , as shown in Fig. 10. All orbital structures in the figure correspond to a prolate Nilsson scheme.  $^{49}\text{V}$  has one less proton than  $^{50}\text{Cr}$ . As a consequence, different  $K^\pi$  bands in  $^{49}\text{V}$  may be obtained by coupling a proton hole of suitable angular momentum to the various  $K^\pi$  bands of  $^{50}\text{Cr}$ . These possibilities are illustrated in Fig. 10. We therefore performed one-nucleon-transfer spectroscopic factor calculation using the shell model to understand the origin of the observed  $K^\pi = 3/2^-$  and  $K^\pi = 15/2^-$  bands in  $^{49}\text{V}$ . The LBSM calculations were performed for  $^{50}\text{Cr}$  using

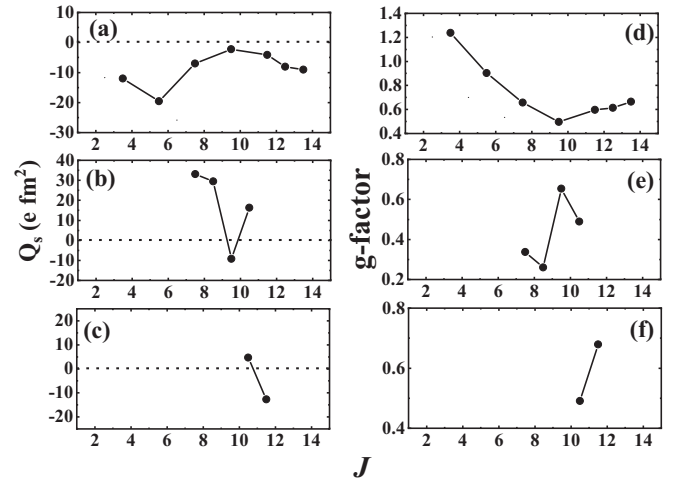


FIG. 9. Calculated spectroscopic quadrupole moment ( $Q_s$ ) of the levels of interest in (a)  $K^\pi = 3/2^-$ , (b)  $K^\pi = 15/2^-$ , and (c)  $K^\pi = 21/2^-$  bands in  $^{49}\text{V}$ . Calculated  $g$  factors of the levels of interest in (d)  $K^\pi = 3/2^-$ , (e)  $K^\pi = 15/2^-$ , and (f)  $K^\pi = 21/2^-$  bands in  $^{49}\text{V}$ . Data points are connected by lines to aid the eye.



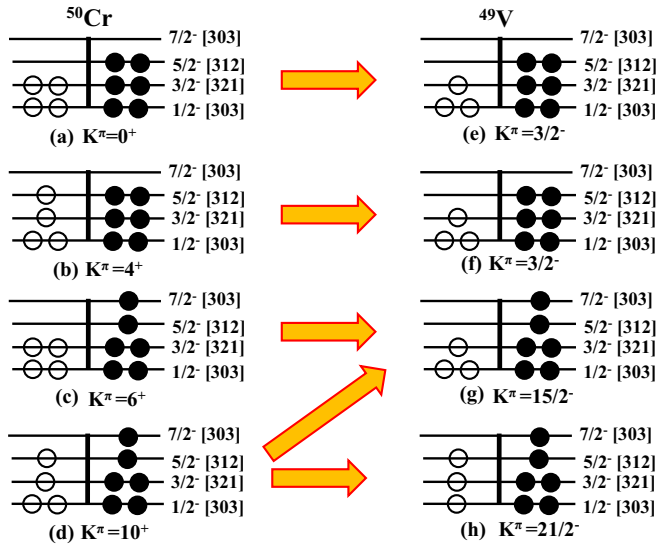


FIG. 10. The orbital structures (in the prolate Nilsson scheme) of protons (open circles) and neutrons (closed circles) in  $^{50}\text{Cr}$  and  $^{49}\text{V}$  with their corresponding  $K^\pi$  values. Arrows indicate the formation of various  $K^\pi$  bands in  $^{49}\text{V}$  as a result of coupling a proton hole to different orbitals of the various  $K^\pi$  bands in  $^{50}\text{Cr}$ .

the code NUSHELLX [31]. The KB3GPN effective interaction [32] was used to carry out these calculations. The model space consists of the full  $pf$  shell for both protons and neutrons. No restriction was applied on any particle in order to generate the levels. A comparison between experimental and calculated energies of the levels in  $^{50}\text{Cr}$  is shown in Fig. 11.

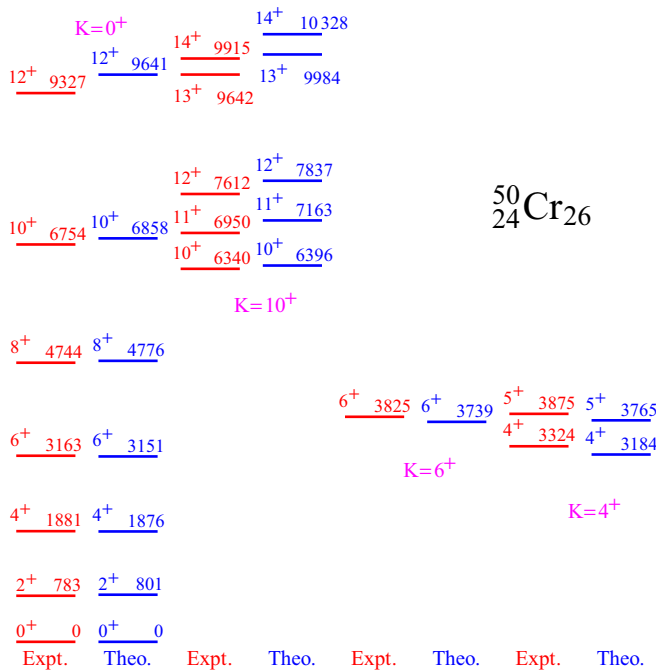


FIG. 11. Comparison of theoretical and experimental positive parity levels in  $^{50}\text{Cr}$ . Only the levels of interest are shown in this figure.

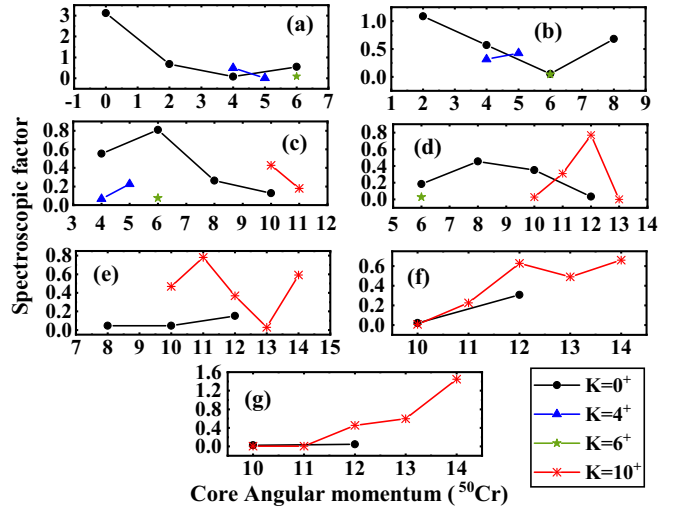


FIG. 12. Calculated spectroscopic factors for (a)  $7/2^-$ , (b)  $11/2^-$ , (c)  $15/2^-$ , (d)  $19/2^-$ , (e)  $23/2^-$ , (f)  $25/2^-$ , and (g)  $27/2^-$  states in  $^{49}\text{V}$  to estimate the contribution of the different  $K^\pi$  bands of the core nucleus,  $^{50}\text{Cr}$ . Data points are connected by lines to aid the eye.

In the calculations, a proton hole in the  $fp$  shell was coupled to the observed  $K^\pi = 0^+, 4^+, 6^+$ , and  $10^+$  bands [35] of  $^{50}\text{Cr}$ , and the spectroscopic factors were extracted from their corresponding wave functions. The results of these calculations are shown in Figs. 12 and 13. From Figs. 12(a), 12(b), and 12(c), we observe that the low-lying  $7/2^-$ ,  $11/2^-$ , and  $15/2^-$  states in  $^{49}\text{V}$  have large spectroscopic factors corresponding to the core angular momentum states  $0_1^+$ ,  $2_1^+$ , and  $6_1^+$  respectively of the  $K^\pi = 0^+$  band. In addition, significant contributions from the  $K^\pi = 4^+$  band were also observed for these states. These contributions show a decreasing trend for states above  $15/2^-$ , for which the  $K^\pi = 10^+$  states dominate [Figs. 12(d)–(g)]. The  $19/2^-$ ,  $23/2^-$ , and  $25/2^-$  states have

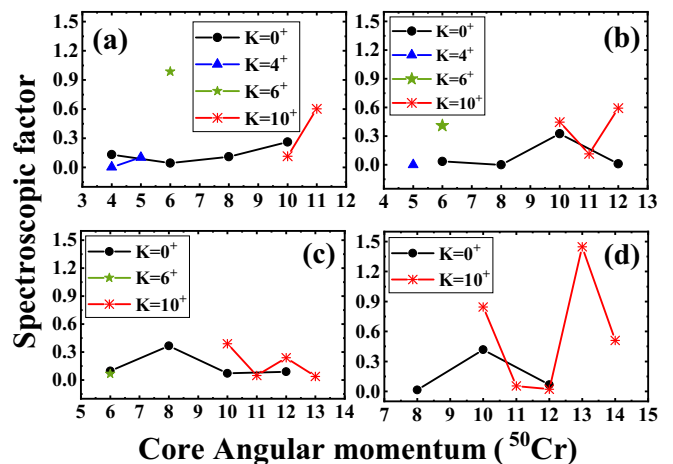


FIG. 13. Calculated spectroscopic factors for (a)  $15/2^-$ , (b)  $17/2^-$ , (c)  $19/2^-$ , and (d)  $21/2^-$  states in  $^{49}\text{V}$  to estimate the contribution of the different  $K^\pi$  bands of the core nucleus,  $^{50}\text{Cr}$ . Data points are connected by lines to aid the eye.

prominent spectroscopic factors corresponding to the core angular momentum states  $12_1^+$ ,  $11_1^+$ , and  $14_1^+$  respectively of the  $K^\pi = 10^+$  band with small yet finite contributions from the  $K^\pi = 0^+$  band. The  $27/2_1^-$  state is solely dominated by the core angular momentum states of the  $K^\pi = 10^+$  band only. It is evident from Fig. 10 that the coupling of a proton hole to the states of the  $K^\pi = 0^+$  or  $4^+$  band in  $^{50}\text{Cr}$  leads to states of the  $K^\pi = 3/2^-$  band in  $^{49}\text{V}$ . Similarly, the coupling of a proton hole to the states of the  $K^\pi = 6^+$  or  $10^+$  band in  $^{50}\text{Cr}$  gives rise to the states of the  $K^\pi = 15/2^-$  band in  $^{49}\text{V}$ . Therefore, the results of Fig. 12 show that, among all the negative parity states of the ground state band in  $^{49}\text{V}$ ,  $7/2_1^-$  and  $11/2_1^-$  states are almost pure  $K^\pi = 3/2^-$  states. Moving up along the ground state band, the contribution from  $K^\pi = 3/2^-$  decreases and becomes insignificant at the band terminating  $J^\pi = 27/2_1^-$  state. The mixing of  $K^\pi = 15/2^-$  with  $K^\pi = 3/2^-$ , therefore, starts from  $J^\pi = 15/2_1^-$ , and becomes maximum at  $J^\pi = 27/2_1^-$ . The calculated  $Q_s$  values and the  $g$  factors of these states also support this observation (Fig. 9).

For the  $K^\pi = 15/2^-$  band in  $^{49}\text{V}$ ,  $15/2_2^-$ ,  $17/2_1^-$ , and  $21/2_1^-$  states have large spectroscopic factors corresponding to the core angular momentum states  $6_2^+$ ,  $12_1^+$ , and  $13_1^+$ , respectively [Figs. 13(a), 13(b), and 13(d)]. In  $^{50}\text{Cr}$ ,  $6_2^+$  state belongs to the  $K^\pi = 6^+$  band, whereas  $12_1^+$  and  $13_1^+$  states belong to the  $K^\pi = 10^+$  band. Interestingly, finite spectroscopic factors corresponding to the core angular momentum states of  $K^\pi = 0^+$  and  $4^+$  bands were also observed for these states of the  $K^\pi = 15/2^-$  band (Fig. 13). However, these contributions are much smaller compared to the contributions from the  $K^\pi = 6^+$  and  $10^+$  bands. We may, therefore, conclude that these states primarily belong to the  $K^\pi = 15/2^-$  band with a small mixing of  $K^\pi = 3/2^-$  band. The calculated positive  $Q_s$  values and the  $g$  factors of these states also support this observation (Fig. 9). However, for the  $19/2_2^-$  state, similar spectroscopic factors, corresponding to the core angular momentum states of  $K^\pi = 0^+$  and  $10^+$  bands, were obtained [Fig. 13(c)]. Thus, a strong mixing between  $K^\pi = 15/2^-$  and  $3/2^-$  is implied for the  $19/2_2^-$  state in  $^{49}\text{V}$ . This strong mixing of the two  $K$  bands is the reason behind the sudden change in the sign of  $Q_s$  at  $19/2_2^-$  [Fig. 9(b)]. To understand the reason for this sudden change, we refer to the  $Q_s$  calculations of Brandolini and Ur [15] done for a pure rotor ( $\beta^* = 0.25$ ). The calculated  $Q_s$  of the  $19/2_2^-$  state is positive in the case of  $K^\pi = 15/2^-$ , whereas it is negative in the case of  $K^\pi = 3/2^-$ . A strong mixing of the  $K^\pi = 3/2^-$  band will pull the  $Q_s$  of the  $K^\pi = 15/2^-$  band down, thus easily explaining the sudden dip of  $Q_s$  and its change of sign at  $19/2_2^-$  in the otherwise smooth trend [Fig. 9 (b)]. In addition, the sudden increase of the  $g$  factor at  $19/2_2^-$  [Fig. 9(e)] also supports the existence of a strong mixing of the two bands at  $19/2_2^-$ .

### C. Total Routhian surface (TRS) calculations

Total Routhian surface (TRS) calculations [36] were carried out to understand the shape of the  $^{49}\text{V}$  nucleus associated with the configurations assigned to the bands of interest. The TRS was calculated at each frequency,  $\omega$  in the  $\beta_2$ - $\gamma$  plane, with minimization on  $\beta_4$ , considering the macroscopic

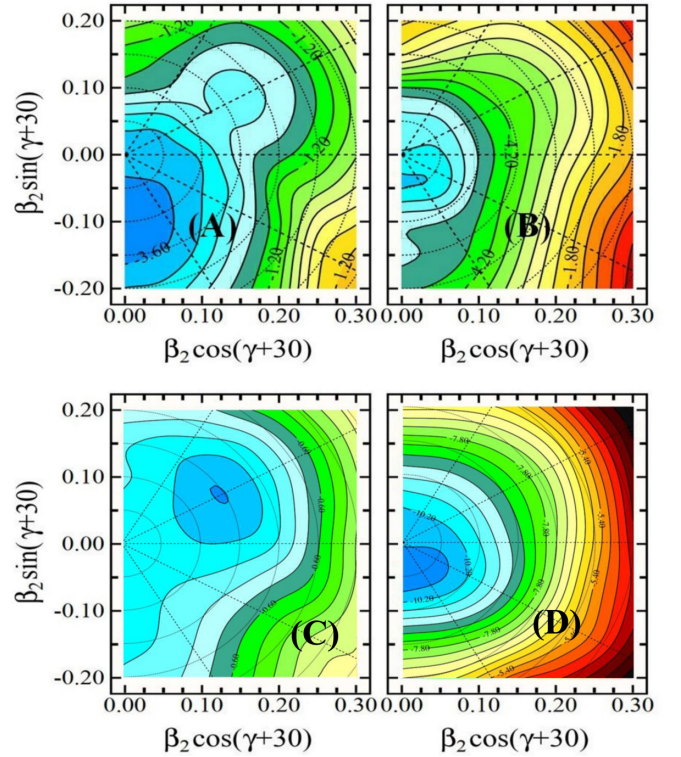


FIG. 14. TRS plots for the negative parity states. In the top row ( $K^\pi = 3/2^-$ ) the plots correspond to (a)  $\omega = 0.55$  and (b)  $0.75$  MeV. In the bottom row ( $K^\pi = 15/2^-$ ), they are calculated for (c)  $\omega = 0.60$  and (d)  $1.15$  MeV.

liquid-drop energy of the nucleus, the shell correction, and the pairing energy. The single-particle energies were obtained from the Woods-Saxon potential and the pairing included a monopole and a double-stretched quadrupole interaction [36]. For the  $K^\pi = 3/2^-$  band, a near-prolate deformation is predicted with  $\beta_2 = 0.10$  at  $\omega = 0.55$  MeV [Fig. 14(a)]. However, at higher frequencies ( $\omega = 0.75$ – $0.95$  MeV), a triaxial shape with a small deformation ( $\beta_2 = 0.05$ ) remains energetically favored [Fig. 14(b)], as predicted in Ref. [15]. For the  $K^\pi = 15/2^-$  band also, a near-prolate deformation is predicted with  $\beta_2 = 0.15$  at  $\omega = 0.6$  MeV, as shown in Fig. 14(c), and at  $\omega = 1.05$  MeV a triaxial shape with a small deformation ( $\beta_2 = 0.04$ ) remains energetically favored. Finally, it terminates with a near-prolate deformation with  $\beta_2 = 0.04$  as shown in Fig. 14(d). As the  $J^\pi = 25/2_1^-$  and  $27/2_1^-$  levels are generated primarily from the  $K^\pi = 15/2^-$  band, we may also conclude that a prolate shape prevails for these states with a small deformation.

Since the  $K$  mixing starts from the  $15/2_1^-$  state, we have plotted (Fig. 15) the single-particle Routhians for (a) protons and (b) neutrons with  $\omega$  at the triaxial minimum ( $\beta_2 = 0.04$  and  $\gamma = -99^\circ$ ). It can be seen from Fig. 15(b) that, at higher  $\omega$  ( $>0.6$ ), Nilsson levels of interest ( $\Omega = 5/2, +$  and  $7/2, -$ ) are very close to each other and the  $\Omega = 7/2, -$  orbital even crosses the  $\Omega = 5/2, +$  orbital at higher frequencies. So, one may expect configuration mixing between these levels. The presence of triaxiality in  $^{49}\text{V}$  therefore leads to the mixing

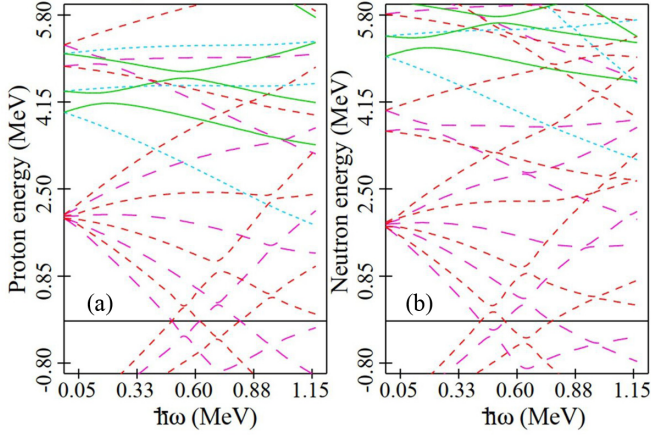


FIG. 15. Single-particle (a) proton and (b) neutron energies in a rotating frame as a function of rotational frequency calculated at deformation parameters  $\beta_2 = 0.04$  and  $\gamma = -99^\circ$ . The four combinations of  $(\pi, \alpha)$  are displayed in the following way: solid green lines represent positive parity positive signature and dotted cyan lines indicate positive parity negative signature. Similarly, negative parity negative signature and negative parity positive signature are represented by magenta and red lines, respectively.

of configurations between different Nilsson levels. Thus, the observed  $K$  mixing between the two negative parity bands arises as a result of configuration mixing between different Nilsson orbitals.

#### D. Identification of a $K^\pi = 21/2^-$ band

In the level scheme of  $^{49}\text{V}$ , a yrare  $21/2_2^-$  state was observed that is connected to  $19/2_1^-$  state of the ground state band through a 2114 keV transition. This state does not decay to any level of the  $K^\pi = 15/2^-$  band. Another yrare  $23/2_2^-$  state was observed that decays via five transitions: to the  $21/2_1^-$  and  $19/2_2^-$  states of the  $K^\pi = 15/2^-$  band through 934 and 2067 keV  $\gamma$ 's, respectively; to the  $23/2_1^-$  and  $19/2_1^-$  states of the ground state band through 777 and 2723 keV  $\gamma$ 's, respectively; and to the above-mentioned yrare  $21/2_2^-$  state through a 609 keV  $\gamma$ . Among these five  $\gamma$ 's, the 609 keV is the most intense transition. As was observed in the  $K^\pi = 15/2^-$  band (Table III), mostly, intraband  $M1$  strengths are comparatively stronger than interband  $M1$  strengths. For the neighboring  $^{50}\text{Cr}$  nucleus also it was found that the observed intraband transitions ( $5^+ \rightarrow 4^+$  and  $10^+ \rightarrow 8^+$ ) are comparatively stronger than the inter-band transitions [35]. Thus, it can be indicated from the present discussion that these two yrare states might not be members of the  $K^\pi = 15/2^-$  band. Rather, these two states may belong to a new band with the 609 keV  $\gamma$  as the intraband transition.

From one-nucleon-transfer spectroscopic factor calculations, it is found that the maximum contribution to the  $21/2_2^-$  state arises from the core angular momentum states  $11^+$  and  $13^+$ , that belong to the  $K^\pi = 10^+$  band in  $^{50}\text{Cr}$  [Fig. 16(a)]. Since the  $21/2_2^-$  state is highly unlikely to be a member of the  $K^\pi = 15/2^-$  band, the  $K^\pi = 10^+$  band in  $^{50}\text{Cr}$  must correspond to a band in  $^{49}\text{V}$  other than the  $K^\pi = 15/2^-$

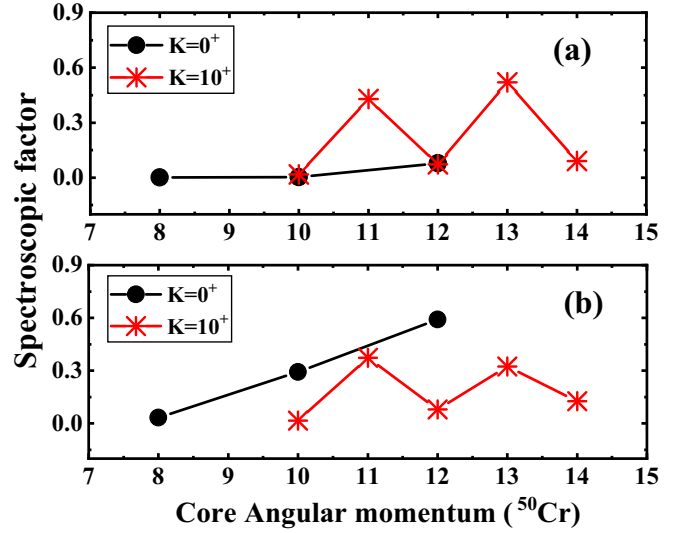


FIG. 16. Calculated spectroscopic factors for (a)  $21/2_2^-$  and (b)  $23/2_2^-$  states in  $^{49}\text{V}$  to estimate the contribution of the different  $K^\pi$  bands of the core nucleus,  $^{50}\text{Cr}$ . Data points are connected by lines to aid the eye.

band. Now, the  $K^\pi = 10^+$  band in  $^{50}\text{Cr}$  may give rise to a  $K^\pi = 21/2^-$  band in  $^{49}\text{V}$ , if the proton hole is coupled to the  $[303]1/2^-$  orbital, instead of coupling to the  $[312]5/2^-$  orbital (Fig. 10). Thus, the  $21/2_2^-$  state may be assigned to a hitherto unassigned  $K^\pi = 21/2^-$  band in  $^{49}\text{V}$ . From the results of spectroscopic factor calculation for the  $23/2_2^-$  state, it is observed that this state has large contributions corresponding to the core angular momentum states  $11^+$  and  $13^+$  of the  $K^\pi = 10^+$  band in  $^{50}\text{Cr}$  [Fig. 16(b)]. Following the same arguments as above, the  $23/2_2^-$  state might also be assigned to the new  $K^\pi = 21/2^-$  band. However, there is a dominant contribution from the  $K^\pi = 0^+$  band of  $^{50}\text{Cr}$  as well [Fig. 16(b)]. This implies a strong mixing of the  $K^\pi = 3/2^-$  band with the  $K^\pi = 21/2^-$  band at the  $23/2_2^-$  state. The calculated  $Q_s$  value (Fig. 9) for the  $21/2_2^-$  state is, therefore, positive, and changes suddenly to a negative value for the  $23/2_2^-$  state. This change of sign and its implication towards a strong mixing between the two bands can be understood again from the  $Q_s$  calculations of Brandolini and Ur [15], as was discussed for the case of the  $19/2_2^-$  state of the  $K^\pi = 15/2^-$  band. Thus, based on the above reasoning, we predict the existence of a  $K^\pi = 21/2^-$  band, with  $21/2_2^-$  and  $23/2_2^-$  states as its members. We also predict that the  $23/2_2^-$  state has a strong mixing with the  $K^\pi = 3/2^-$  band.

## VI. CONCLUSION

Negative parity bands of  $^{49}\text{V}$ , populated through  $^{48}\text{Ti}(^4\text{He}, 2np)^{49}\text{V}$  reaction with a 48 MeV  $^4\text{He}$  beam, were studied using the Indian National Gamma Array (INGA) facility. We measured multipole mixing ratios of ten transitions, out of which eight were measured for the first time. The lifetimes of four levels were measured for the first time. In addition to that, seven level lifetimes were remeasured and compared with their earlier measurements.

Large basis shell model calculations were performed to understand the microscopic origin of these levels, and to interpret the observations. The presence of  $K$  mixing in  $^{49}\text{V}$  was established from one-nucleon-transfer spectroscopic factor calculations and TRS calculations. Based on the results obtained from the experiment and shell model calculations, a new  $K^\pi = 21/2^-$  band is predicted in the existing level scheme.

### ACKNOWLEDGMENTS

The authors sincerely thank Mr. P. K. Das (Saha Institute of Nuclear Physics) for the preparation of the target. The XRF facility of Department of Physics, IEST Shibpur, used for

target characterization, is also acknowledged. Special thanks are due to the accelerator staff of VECC, Kolkata for a nearly uninterrupted beam. We would also like to thank all the members of the INGA (partially funded by the Department of Science and Technology, Government of India) collaboration. Y.S. acknowledges the financial support in the form of an INSPIRE fellowship provided by the Department of Science and Technology, Ministry of Science and Technology, Govt. of India, Contract. No. DST/INSPIRE Fellowship/IF160573. One of the authors (A.B.) would like to express his deep gratitude towards SERB-DST India (Project No. EMR/2016/006339) for financial support. A.B. and Y.S. would also like to thank Prof. M. Saha Sarkar (Saha Institute of Nuclear Physics) for her valuable suggestions and fruitful discussions during the course of the work.

- 
- [1] S. M. Lenzi, in *Nuclear Physics with Stable and Radioactive Ion Beams*, Proceedings of the International School of Physics “Enrico Fermi”, edited by F. Gramegna, P. Van Duppen, A. Vitturi, and S. Pirrone (IOS, Amsterdam, 2019).
- [2] S. M. Lenzi, C. A. Ur, D. R. Napoli, M. A. Nagarajan, D. Bazzacco, D. M. Brink, M. A. Cardona, G. de Angelis, M. De Poli, A. Gadea, D. Hojman, S. Lunardi, N. H. Medina, and C. Rossi Alvarez, *Phys. Rev. C* **56**, 1313 (1997).
- [3] S. M. Lenzi, D. R. Napoli, A. Gadea *et al.*, High spin states in  $^{48}\text{Cr}$ , *Z. Phys. A* **354**, 117 (1996).
- [4] J. A. Cameron *et al.*, *Phys. Lett. B* **387**, 266 (1996).
- [5] J. A. Cameron, M. A. Bentley, A. M. Bruce, R. A. Cunningham, W. Gelletly, H. G. Price, J. Simpson, D. D. Warner, and A. N. James, *Phys. Rev. C* **49**, 1347 (1994).
- [6] E. Caurier, J. L. Egido, G. Martínez-Pinedo, A. Poves, J. Retamosa, L. M. Robledo, and A. P. Zuker, *Phys. Rev. Lett.* **75**, 2466 (1995).
- [7] E. Caurier, A. P. Zuker, A. Poves, and G. Martínez-Pinedo, *Phys. Rev. C* **50**, 225 (1994).
- [8] J. A. Cameron *et al.*, *Phys. Lett. B* **319**, 58 (1993).
- [9] F. Brandolini *et al.*, *Nucl. Phys. A* **642**, 387 (1998).
- [10] C. E. Svensson, S. M. Lenzi, D. R. Napoli, A. Poves, C. A. Ur, D. Bazzacco, F. Brandolini, J. A. Cameron, G. de Angelis, A. Gadea, D. S. Haslip, S. Lunardi, E. E. Maqueda, G. Martínez-Pinedo, M. A. Nagarajan, C. Rossi Alvarez, A. Vitturi, and J. C. Waddington, *Phys. Rev. C* **58**, R2621 (1998).
- [11] A. Juodagalvis, I. Ragnarsson, and S. Åberg, *Phys. Lett. B* **477**, 66 (2000).
- [12] E. Caurier, G. Martínez-Pinedo, F. Nowacki, A. Poves, and A. P. Zuker, *Rev. Mod. Phys.* **77**, 427 (2005).
- [13] A. P. Zuker, *Phys. Rev. Lett.* **90**, 042502 (2003).
- [14] G. Martínez-Pinedo, A. Poves, L. M. Robledo, E. Caurier, F. Nowacki, J. Retamosa, and A. Zuker, *Phys. Rev. C* **54**, R2150 (1996).
- [15] F. Brandolini and C. A. Ur, *Phys. Rev. C* **71**, 054316 (2005).
- [16] D. Rodrigues, D. Hojman, S. M. Lenzi, M. A. Cardona, E. Farnea, M. Axiotis, C. Beck, P. Bednarczyk, P. G. Bizzetti, A. M. Bizzetti-Sona, F. Della Vedova, J. Grębosz, F. Haas, M. Kmiecik, A. Maj, W. Męczyński, D. R. Napoli, M. Nespolo, P. Papka, A. S. Zafra, J. Styczen, S. Thummerer, and M. Ziębliński, *Phys. Rev. C* **92**, 024323 (2015).
- [17] S. Mukhopadhyay *et al.*, *Nucl. Phys. A* **1000**, 121785 (2020).
- [18] S. Das *et al.*, *Nucl. Instrum. Methods Phys. Res., Sect. A* **893**, 138 (2018).
- [19] R. Bhowmick *et al.*, Proc. DAE-BRNS Symp. Nucl. Phys. (India) **B 44**, 422 (2001).
- [20] A. Bisoi, M. S. Sarkar, S. Sarkar, S. Ray, D. Pramanik, R. Kshetri, S. Nag, K. Selvakumar, P. Singh, A. Goswami, S. Saha, J. Sethi, T. Trivedi, B. S. Naidu, R. Donthi, V. Nanal, and R. Palit, *Phys. Rev. C* **89**, 024303 (2014).
- [21] A. Gavron, *Phys. Rev. C* **21**, 230 (1980).
- [22] E. S. Macias, W. D. Ruhter, D. C. Camp, and R. G. Lanier, *Comput. Phys. Commun.* **11**, 75 (1976).
- [23] B. Haas, J. Chevallier, J. Britz, and J. Styczen, *Phys. Rev. C* **11**, 1179 (1975).
- [24] K. Starosta, T. Morek, Ch. Droste, S. G. Rohoziński, J. Srebrny, A. Wierchucka, M. Bergström, B. Herskind, E. Melby, T. Czosnyka, and P. J. Napiorkowski, *Nucl. Instrum. Methods A* **423**, 16 (1999).
- [25] A. Das *et al.*, *Phys. Rev. C* **101**, 044310 (2020).
- [26] J. C. Wells and N. R. Johnson, Oak Ridge National Laboratory (ORNL) Physics Division Progress Report ORNL-6689, 1991, p. 44; R. K. Bhowmik (private communication).
- [27] L. C. Northcliffe and R. F. Schilling, *At. Data Nucl. Data Tables* **7**, 233 (1970).
- [28] C. M. Rozsa, R. G. Arns, B. J. Brunner, S. E. Caldwell, and J. W. Smith, *Bull. Am. Phys. Soc.* **17**, 536 (1972); Z. P. Sawa, J. Blomqvist, and W. Gullholmer, *Nucl. Phys. A* **205**, 257 (1973).
- [29] S. L. Tabor and R. W. Zurmühle, *Phys. Rev. C* **10**, 35 (1974).
- [30] A. Kiuru, *Z. Phys.* **251**, 93 (1972).
- [31] NuShellX@MSU, B. A. Brown, W. D. M. Rae, E. McDonald, and M. Horoi, <http://www.nsl.msui.edu/~brown/resources/resources.html>; NuShellX, W. D. M. Rae, <http://www.garsington.eclipse.co.uk/>
- [32] A. Poves, J. Sánchez-Solano, E. Caurier, and F. Nowacki, *Nucl. Phys. A* **694**, 157 (2001).
- [33] C. A. Ur, D. Bucurescu, S. M. Lenzi, G. Martínez-Pinedo, D. R. Napoli, D. Bazzacco, F. Brandolini, D. M. Brink, J. A. Cameron, E. Caurier, G. de Angelis, M. De Poli, A. Gadea, S. Lunardi, N. Mărginean, M. A. Nagarajan, P. Pavan, C. Rossi Alvarez, and C. E. Svensson, *Phys. Rev. C* **58**, 3163 (1998).

- [34] F. Brandolini, N. Märginean, S. Hankonen, N. H. Medina, R. V. Ribas, J. Sanchez-Solano, S. M. Lenzi, S. Lunardi, D. R. Napoli, A. Poves, C. A. Ur, D. Bazzacco, G. de Angelis, M. De Poli, E. Farnea, A. Gadea, T. Martinez, and C. Rossi-Alvarez, *Phys. Rev. C* **66**, 024304 (2002).
- [35] F. Brandolini, J. Sanchez-Solano, S. M. Lenzi, N. H. Medina, A. Poves, C. A. Ur, D. Bazzacco, G. De Angelis, M. De Poli, E. Farnea, A. Gadea, D. R. Napoli, and C. Rossi-Alvarez, *Phys. Rev. C* **66**, 021302(R) (2002).
- [36] W. Nazarewicz, J. Dudek, R. Bengtsson, T. Bengtsson, and I. Ragnarsson, *Nucl. Phys. A* **435**, 397 (1985); W. Nazarewicz, M. A. Riley, and J. D. Garrett, *ibid.* **512**, 61 (1990).